THE JOURNAL OF PHYSICAL CHEMISTRY Letters

Letter

pubs.acs.org/JPCL

Construction of Compact Methylammonium Bismuth Iodide Film Promoting Lead-Free Inverted Planar Heterojunction Organohalide Solar Cells with Open-Circuit Voltage over 0.8 V

Chenxin Ran,[†] Zhaoxin Wu,*[,†] Jun Xi, Fang Yuan, Hua Dong, Ting Lei, Xin He, and Xun Hou

Key Laboratory of Photonics Technology for Information, Key Laboratory for Physical Electronics and Devices of the Ministry of Education, School of Electronic and Information Engineering, Xi'an Jiaotong University, Xi'an 710049, PR China

Supporting Information

ABSTRACT: A bismuth-based organohalide material, methylammonium bismuth iodide ($MA_3Bi_2I_9$), has been recently explored as an efficient lead-free light absorber in photovoltaic applications. However, the poor surface morphology of the $MA_3Bi_2I_9$ film fabricated via conventional one-step spin-coating methods has limited the performance of the device. In this work, a smooth, uniform, and compact $MA_3Bi_2I_9$ thin film was realized by a novel two-step evaporation−spin-coating film fabrication strategy for the first time. Taking advantage of the superior $MA_3Bi_2I_9$ thin film, the best-performing inverted planar heterojuncion photovoltaic device exhibited a power conversion efficiency of 0.39% with open-circuit voltage as high as 0.83 V, which demonstrated the lowest loss-in-potential to date in $MA_3Bi_2I_9$-based solar cells. Moreover, the facile film fabrication strategy utilized in this work paves the way for high reproducibility of lead-free organohalide films and devices.

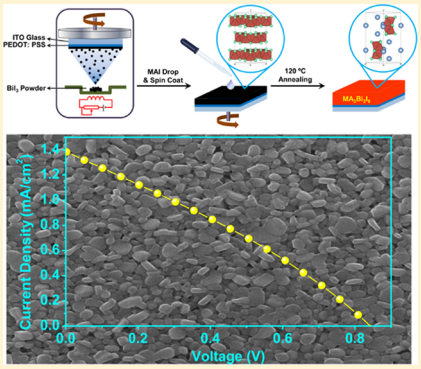

Organic−inorganic hybrid perovskite-type light-absorbing materials, typically $CH_3NH_3PbI_3$, have been widely studied as an efficient active layer in solar cells since the first application in dye-sensitized solar cell (DSSC) in 2009.[1] Over the past few years, great efforts has been made in this field, and the power conversion efficiency (PCE) of the planar heterojuncion (PHJ) perovskite solar cell has rapidly reached 21.6% with promising device stability by element doping.[2] To date, the highest performance of PHJ perovskite solar cells has been obtained using lead (Pb) as the core element, which is well-known to be toxic to the environment and harmful to human health, which may limit its large-scale industrial application.[3] In addition, the instability of lead-based perovskite materials remains a big challenge.[4] As a result, researchers have attempted to develop other lead-free perovskites for photovoltaic application. For example, tin (Sn), which is located in the same main group with Pb, is first used to replace Pb in the perovskite structure.[5] However, Sn^{2+} is considered to be easily oxidized into Sn^{4+}, which makes it difficult to obtain a stable solar cell device.[5] Although introducing SnF_2 and pyrazine into the $FASnI_3$ film could effectively stabilize the film, the open-circuit voltage (V_{oc}) in such a device is still low (~0.3 V), and new strategies are needed to further improve the device performance.[6] In addition to optimizing the film fabrication technique, developing more lead-free metal cores in perovskite materials other than Sn would also be beneficial.

Recently, environment friendly and chemically stable bismuth (Bi)-based methylammonium bismuth iodide $MA_3Bi_2I_9$ organohalide material, which contains post-transition metal Bi^{3+} with a $6s^2$ valence electronic configuration like Pb^{2+}, has been investigated both theoretically and experimentally as a novel lead-free light absorber in optoelectronic applications.[7−15] In these works, a mesoporous device structure of glass/fluorine doped tin oxide (FTO)/compact-TiO_2/mesoscopic-TiO_2/$MA_3Bi_2I_9$/hole transport material(HTM)/Ag was always used, although one recent work applied inverted PHJ structure of glass/indium tin oxide (ITO)/PEDOT:PSS/$MA_3Bi_2I_9$/PCBM/Ca/Al.[12] Nevertheless, the overall PCEs of the $MA_3Bi_2I_9$-based solar cells so far are still low, which is most likely caused by the poor film morphology fabricated via the one-step spin-coating method.[7−15] To overcome this problem, it is of great importance to develop other effective strategies to promote the film quality as well as the device performance.

For lead-based perovskite film, a two-step metal salt evaporation technique has been proven to be an effective strategy that yields a highly efficient device.[16−20] However, the evaporation technique has not been applied in the fabrication of lead-free organohalide films to date. In this work, a smooth, continuous, and compact $MA_3Bi_2I_9$ thin film composed of continuous $MA_3Bi_2I_9$ grains has been realized for the first time by using a facile two-step fabrication method, including thermal evaporation of BiI_3, spin-coating with MAI solution, and postannealing steps as shown in Scheme 1. The facile film deposition method obtained the compact $MA_3Bi_2I_9$ thin film with a root-mean-square (RMS) roughness of only 13.23 nm. By optimizing the film thickness, concentration of MAI solution, and postannealing conditions, we were able to obtain the best-performing

Received: November 4, 2016
Accepted: January 3, 2017
Published: January 3, 2017

DOI: 10.1021/acs.jpclett.6b02578
J. Phys. Chem. Lett. 2017, 8, 394−400

Scheme 1. Fabrication Procedure of $MA_3Bi_2I_9$ Thin Film

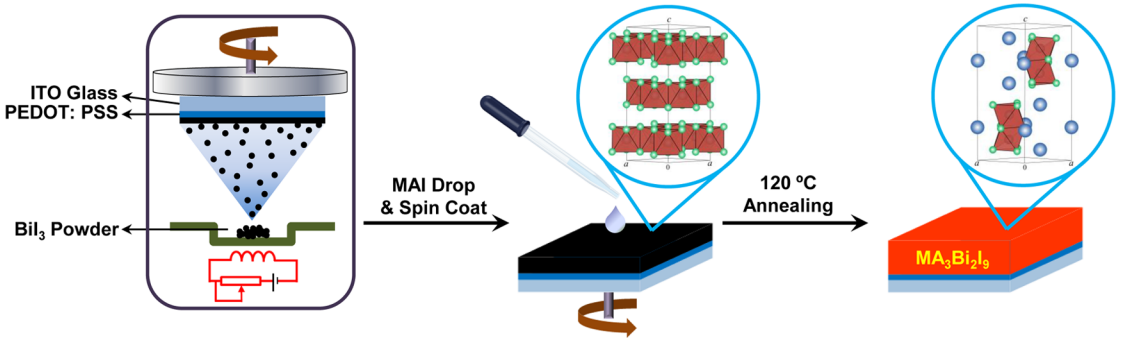

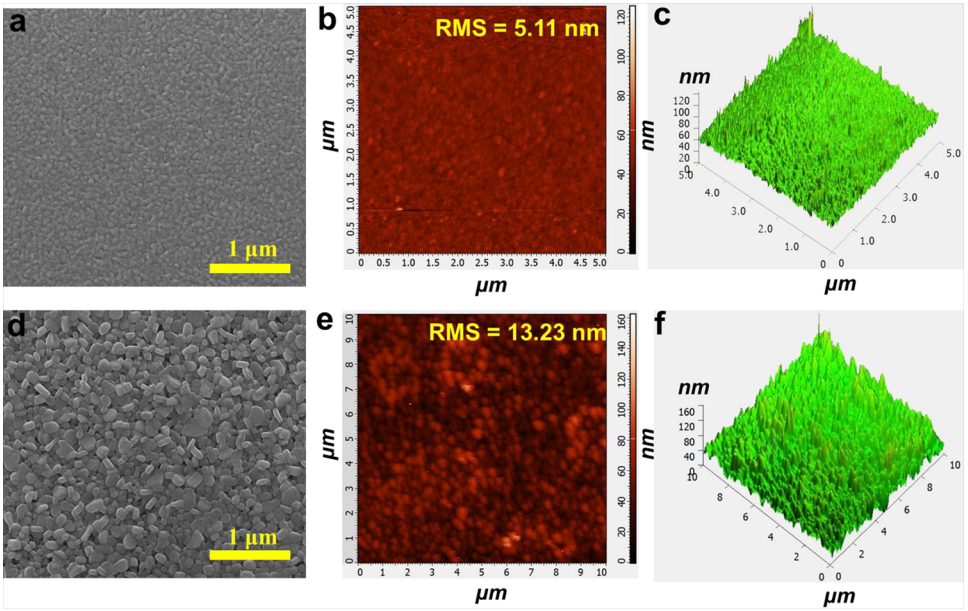

Figure 1. (a) SEM, (b) tapping-mode AFM, and (c) 3D AFM images of evaporated BiI_3 film; (d) SEM, (e) tapping-mode AFM, and (f) 3D AFM images of $MA_3Bi_2I_9$ film.

$MA_3Bi_2I_9$-based lead-free inverted PHJ organohalide solar cells with short-circuit current (J_{sc}), V_{oc}, and PCE as high as 1.39 mA/cm^2, 0.83 V, and 0.39%, respectively.

We fabricated $MA_3Bi_2I_9$ thin films by thermal evaporation of BiI_3 and spin-coating MAI solution to form BiI_3/MAI stacking layer first, and in situ formation of $MA_3Bi_2I_9$ would occur upon postannealing through a molecule interdiffusion process.[21,22] Figure 1 shows the surface morphology of the thermal evaporated BiI_3 film (Figure 1a–c) and the as-prepared $MA_3Bi_2I_9$ film (Figure 1d–f) from scanning electron microscopy (SEM) and atomic force microscopy (AFM). The thermal evaporation technique resulted in a dense and flat BiI_3 thin film. After the spin-coating of MAI on BiI_3 and the postannealing process, uniform and pinhole-free $MA_3Bi_2I_9$ thin film with continuous crystal grains was observed, as shown in Figure 1d. SEM images under lower magnification demonstrated the large-scale uniformity of both BiI_3 and $MA_3Bi_2I_9$ film (Figure S1). A statistical analysis of the top-down resistance after the deposition of Ag contact at different positions of $MA_3Bi_2I_9$ film showed little difference (Figure S2), which suggested a uniform and pinhole-free film. From tapping-mode and the corresponding three-dimensional (3D) AFM characterization, we can see that the RMS roughness values of the BiI_3 and $MA_3Bi_2I_9$ thin films were only 5.11 nm (Figure 1b) and 13.23 nm (Figure 1e), respectively. Such distinguishing $MA_3Bi_2I_9$ thin film is superior to the film made from conventional one-step spin-coating method,[7−15] especially the one made on PEDOT:PSS substrate, where the crystallization process of $MA_3Bi_2I_9$ crystal was quick, leading to the nonuniform film with island morphology.[12]

The XRD patterns of evaporated BiI_3 and as-prepared $MA_3Bi_2I_9$ thin films are shown in Figure 2a. Evaporated BiI_3 film showed its (006) peak at 26°, which indicated that the evaporated BiI_3 film had a preferred orientation with its (006) crystal plane parallel to the substrate owing to the two-dimensional layered crystal structure of BiI_3 (Scheme 1).[23] The peaks at 12.84°, 16.58°, and 24.82° of the $MA_3Bi_2I_9$ film corresponded to (101), (004), and (006) planes of $MA_3Bi_2I_9$ crystal according to the calculated XRD pattern of $MA_3Bi_2I_9$ material,[10] which showed the typical hexagonal space group *P*63/*mmc*.[12] However, there are some differences between the measured and the calculated XRD patterns of the $MA_3Bi_2I_9$ material. The preferred orientation of BiI_3 led to a restrained growth of $MA_3Bi_2I_9$ with preferred orientation; hence, only preferred orientation facets can be detected by XRD measurement. To verify the successful formation of $MA_3Bi_2I_9$ material, we fabricated a thicker $MA_3Bi_2I_9$ thin film via three film fabrication cycles, and more typical peaks of $MA_3Bi_2I_9$ material were monitored, as shown in Figure S3. The reason may be as follows: when the second and third BiI_3

DOI: 10.1021/acs.jpclett.6b02578
J. Phys. Chem. Lett. 2017, 8, 394−400

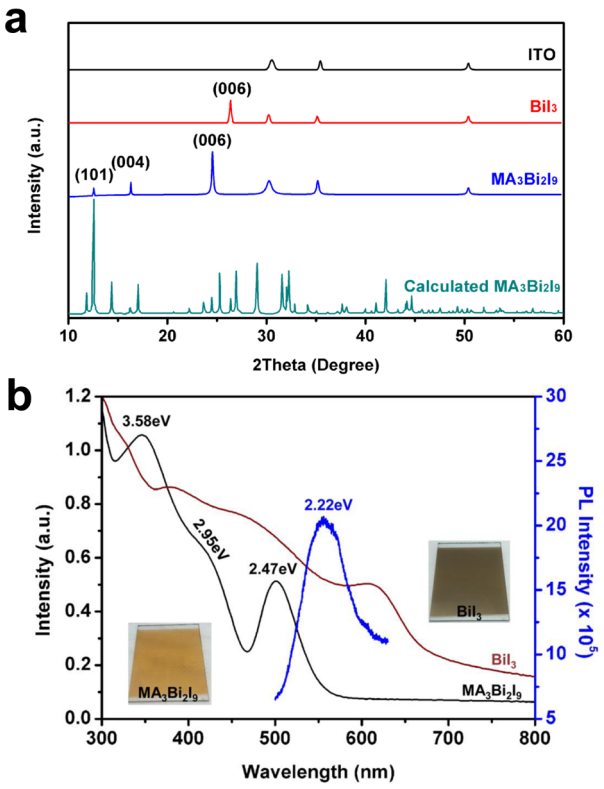

Figure 2. (a) XRD pattern of BiI_3 and $MA_3Bi_2I_9$ films and (b) UV−vis spectra of BiI_3 and $MA_3Bi_2I_9$ films and PL spectra of $MA_3Bi_2I_9$ film. Insets in panel b show photographs of the two films.

layers were evaporated, the surface morphology was different from the first BiI_3 layer on ITO, which led to the natural crystal growth of $MA_3Bi_2I_9$ without obvious preferred orientation. Therefore, a thicker $MA_3Bi_2I_9$ film made from multiple cycles showed XRD patterns matching the calculated result.

Ultraviolet−visible (UV−vis) spectra of BiI_3 and $MA_3Bi_2I_9$ thin films and the PL spectra of $MA_3Bi_2I_9$ film are shown in Figure 2b. The evaporated black BiI_3 film (the inset image in Figure 2b) showed a broad absorption response through the visible-light range from 300 to 650 nm. We use the Tauc plot versus the energy of light to fit a linear absorption edge in a function of $(\alpha h\nu)^{1/2}$ versus $h\nu$[24] (Figure S4) and find that the band gap of the evaporated BiI_3 film was ∼1.82 eV, agreeing well with the reported result.[25] After the transformation into $MA_3Bi_2I_9$, the color of the film turned into light orange, as shown in the inset image of Figure 2b. Because the thickness of the $MA_3Bi_2I_9$ film was low, the color of the film was lighter than that reported in the literature.[7,9,10,12,13] A thicker $MA_3Bi_2I_9$ film showed deeper orange color and enhanced absorption spectra that are in agreement with the literature,[7,9,10,12,13] demonstrating the successful formation of $MA_3Bi_2I_9$ (Figure S5). UV−vis spectra of $MA_3Bi_2I_9$ showed a strong exciton absorption peak at 2.47 eV together with two more absorption bands at 2.95 and 3.58 eV, which was explained as the electron transitions from the ground $^1S_0$ to the excited $^3P_1$, $^3P_2$, and $^1P_1$ states of Bi^{3+} in the isolated $Bi_2I_9^{3-}$ cluster when light energy increased.[10,12,26] No characteristic absorption band of BiI_3 was observed in $MA_3Bi_2I_9$ film, which indicated the complete conversion of BiI_3. The band gap of $MA_3Bi_2I_9$ film obtained from Figure S4 was ∼2.22 eV, which was close to the calculated bandgap of

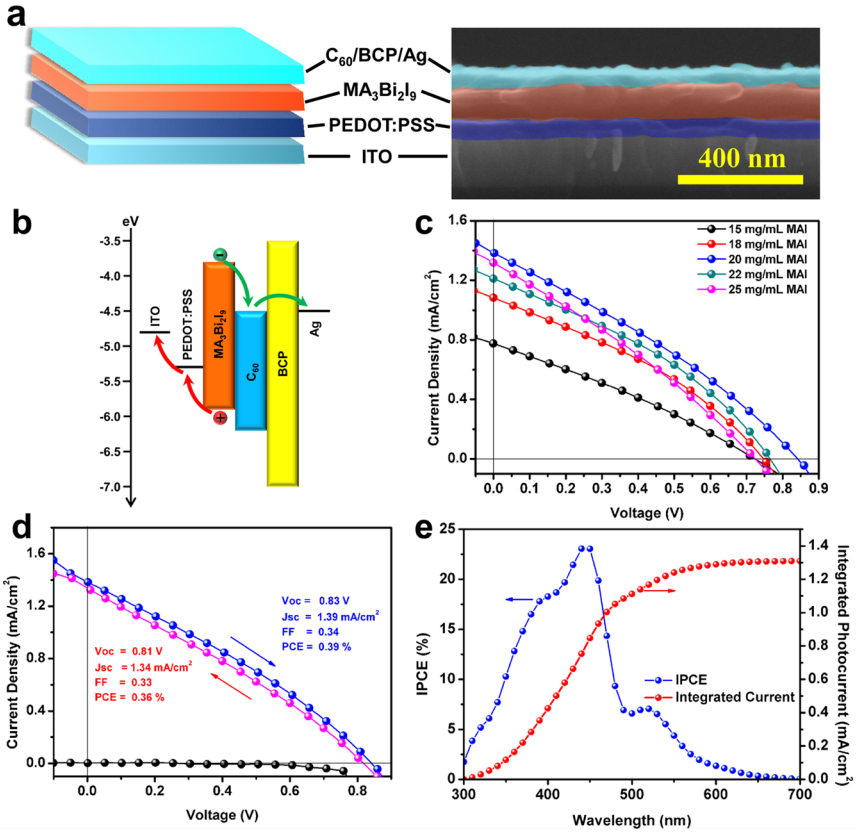

Figure 3. (a) Device structure, cross-sectional SEM image, and (b) energy level diagram of the $MA_3Bi_2I_9$-based perovskite solar cell; (c) device performances with different MAI concentration; (d) forward and backward scanning and (e) IPCE spectra of the best-forming device.

DOI: 10.1021/acs.jpclett.6b02578
J. Phys. Chem. Lett. 2017, 8, 394−400

$MA_3Bi_2I_9$ (2.25 eV)[11] and matched the center position of the PL peak of $MA_3Bi_2I_9$ thin film, as shown in Figure 2b.

Next, we fabricated the PHJ solar cells using $MA_3Bi_2I_9$ thin film as light absorber to explore its photovoltaic performance. Figure 3a shows the stacked device structure and the corresponding cross-sectional SEM image of the $MA_3Bi_2I_9$ organohalide solar cell device in an inverted configuration of ITO/PEDOT:PSS/$MA_3Bi_2I_9$/C_{60}/BCP/Ag. Figure 3b shows the energy level diagram of the device. In the two-step evaporation/spin-coating film fabrication process, the thickness of the evaporated BiI_3, concentration of MAI solution, and the postannealing conditions are the crucial factors to determine the performance of the final device. It is well-known that a thicker film absorbs more light and thus yields a larger photocurrent, but a too-large thickness causes loss of photovoltage and charge transport, most likely due to the increased charge recombination.[21,22] Therefore, the optimization of $MA_3Bi_2I_9$ thin film is crucial to achieving the highest photovoltaic device performance. The effect of the MAI concentration on the device performance was investigated, as shown in Figure 3c. When the concentration of MAI solution reached 20 mg/mL, the V_{oc} and J_{sc} of the devices had the optimized maximum values, which could be explained by the full transformation of BiI_3 into $MA_3Bi_2I_9$ material with no impurity when an appropriate MAI solution concentration was used. Table 1 collects the experimental results from Figure 3c.

Table 1. Performance Parameters of Perovskite Solar Cells with Different MAI Concentrations[a]

MAI conc. (mg/mL)	V_{OC} (V)	J_{SC} (mA/cm^2)	FF	PCE (%)
15	0.72 ± 0.1	0.78 ± 0.07	0.33 ± 0.2	0.17 ± 0.03
18	0.75 ± 0.2	1.08 ± 0.06	0.36 ± 0.1	0.26 ± 0.02
20	0.81 ± 0.2	1.31 ± 0.08	0.35 ± 0.2	0.36 ± 0.03
22	0.76 ± 0.1	1.20 ± 0.06	0.35 ± 0.2	0.33 ± 0.02
25	0.72 ± 0.2	1.26 ± 0.05	0.34 ± 0.1	0.30 ± 0.02

[a]Average and standard deviation values were obtained based on 16 cells for 20 mg/mL and 8 cells for others.

Moreover, a slight hysteresis effect can be observed by comparing the forward and backward scanning $J-V$ curves in Figure 3d. The current density for the best-performing perovskite solar cells was confirmed by comparing the integrated current from the incident photon-to-current conversion efficiency (IPCE) measurements in Figure 3e. We tried to further optimize other film formation conditions, including the thickness of BiI_3 film (Figure 4a), the postannealing conditions (Figure 4b,c) and the fabrication cycles of $MA_3Bi_2I_9$ layer (Figure 4d). The optimized device fabrication conditions are as follows: evaporating 60 nm BiI_3 on PEDOT:PSS substrate, then spin-coating 20 mg/mL MAI solution on substrate under room temperature at 4000 rpm for 30 s, followed by postannealing for 3 h at 120 °C. The parameters of the best-performing device are J_{sc} = 1.39 mA/cm^2, V_{oc} = 0.83 V, FF = 0.34, and PCE = 0.39%. Here, J_{sc} and V_{oc} are the highest value among the state-of-art $MA_3Bi_2I_9$-based lead-free organohalide solar cells to date, as listed in Table S1. Moreover, the film fabrication strategy showed a good reproducibility as shown in Figure S6, and all the devices we fabricated (over 50 devices) were not short-cut.

As shown in Figure 4, optimizing the film fabrication conditions failed to improve the FF of the device, and we tried to determine the reason for this result. Previous work showed that the exciton binding energy of $MA_3Bi_2I_9$ thin film was estimated to be ~70 meV,[7] which was higher than that of the Pb-based perovskite materials (~20 meV).[26] The high exciton binding energy would make it much easier for charge to recombine, which could limit the FF of the device. In addition to exciton binding energy, the carrier diffusion ability of the light absorber also determined the FF of the solar cell device. To investigate the carrier diffusion ability of $MA_3Bi_2I_9$ thin film, we conducted the PL characterization in Figure 5a,b. Comparison of measurements on bare $MA_3Bi_2I_9$ against $MA_3Bi_2I_9$/hole acceptor (PEDOT:PSS) bilayers and $MA_3Bi_2I_9$/electron acceptor (C_{60}) bilayers enables identification of electron and hole signatures in the $MA_3Bi_2I_9$ film.[27] The PL quenching effect, which revealed the charge-transfer process at the film interface, could be observed when $MA_3Bi_2I_9$ was interfaced with PEDOT:PSS or C_{60}. It can be seen that C_{60} showed a more efficient electron extraction ability than that of PEDOT:PSS for hole extraction, as shown in Figure 5a. By further comparing the PL decay lifetime in the presence and absence of the quenching layers, the exciton diffusion length, L_D, for electrons and holes can be estimated.[28−30] When the thickness of the film is less than its absorption length, an average PL lifetime in the presence of interfacial quenching, τ_q, can be estimated as[27]

$$\tau_q \approx \tau[1 + \pi^2/8(L_D/L)^2]^{-1} \quad (1)$$

where τ is the PL lifetime of film without interfacial quencher, L_D the exciton diffusion length, and L the thickness of the film. Equation 1 provides a very useful expression to easily approximate L_D from the transient PL decay data, especially if the data fits well to a single-exponential function. Using the fitted τ_q and the known film thickness, L, L_D can be estimated by

$$L_D \approx 2L/\pi[2(\tau/\tau_q - 1)]^{0.5} \quad (2)$$

The PL decay spectra of $MA_3Bi_2I_9$ film with and without interfacial layer are shown in Figure 5b, and the lifetimes fitted by single-exponential function are 0.78, 0.75, and 0.66 ns for bare $MA_3Bi_2I_9$, $MA_3Bi_2I_9$/PEDOT:PSS, and $MA_3Bi_2I_9$/C_{60}, respectively. Here, the thickness of the $MA_3Bi_2I_9$ film was ~120 nm based on the cross-sectional SEM image in Figure 3a; therefore, the diffusion lengths, L_D, for electron and hole calculated by eq 2 are 46.0 and 21.6 nm, respectively, which are lower than those of the Pb-based perovskite thin film (>100 nm).[28] This relatively short exciton diffusion length may be partially responsible for the low FF in the device.

Another critical factor detrimental to solar cell performance was charge carrier trapping effect, which introduced competitive recombination channels.[31] The charge carrier trap-state density should be necessarily low for a highly efficient solar cell, while high trap-state density leads to high charge recombination probability. We therefore fabricated an ITO/$MA_3Bi_2I_9$/Ag device to measure the carrier trap-state density and charge mobility in the $MA_3Bi_2I_9$ thin film as shown in space charge limited current (SCLC) measurement in Figure 5c. The linear fitting (green) indicates an ohmic response of the device at low bias voltage, and a steep increase (yellow) when the bias voltage exceeds the trap-filled limit voltage (V_{TFL}), demonstrating that the trap states are completely filled at this voltage. The trap-state density in the film can be estimated by[10]

$$n_{trap} = 2\varepsilon_0\varepsilon V_{TFL}/qL^2 \quad (3)$$

where ε_0 is the vacuum permittivity, ε the static dielectric constant of $MA_3Bi_2I_9$ (~46),[32] and q the elemental charge. The trap-state density of $MA_3Bi_2I_9$ thin film is calculated to be

DOI: 10.1021/acs.jpclett.6b02578
J. Phys. Chem. Lett. 2017, 8, 394−400

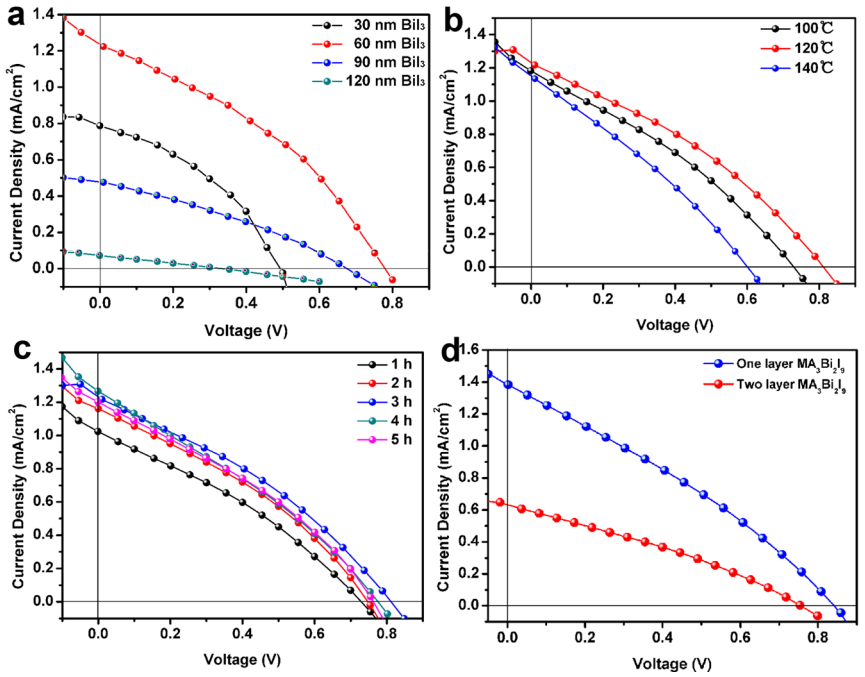

Figure 4. $J-V$ curves of the solar cell devices with different (a) BiI_3 thickness, (b) postannealing temperatre, (c) postannealing time, and (d) $MA_3Bi_2I_9$ film fabrication cycles.

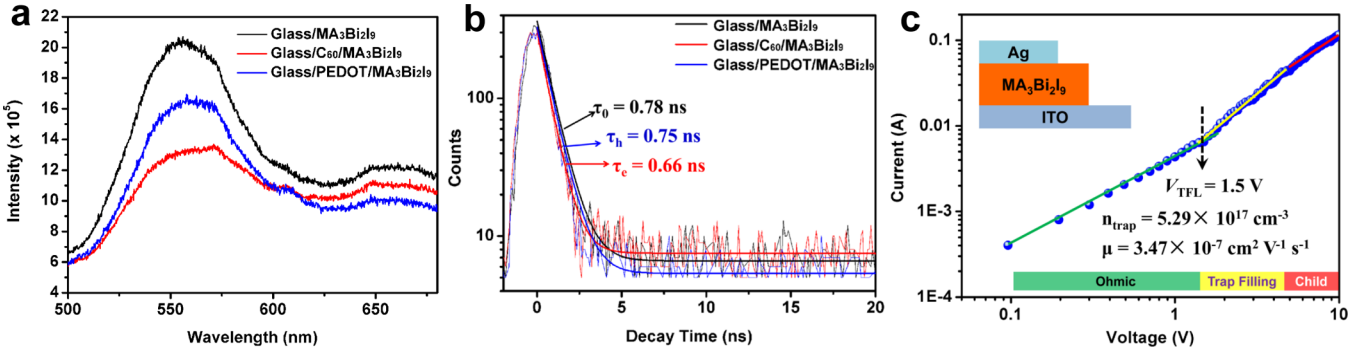

Figure 5. (a) PL and (b) PL decay spectra of $MA_3Bi_2I_9$ film with different substrate; (c) current–voltage curve of the ITO/$MA_3Bi_2I_9$/Ag device on a double-logarithmic scale.

5.29×10^{17} cm^{-3}, which is approximately 1 order of magnitude higher than that of Pb-based perovskite thin film.[33−35] The charge mobility, μ, of film is extracted from Child's regime, which is fitted by the Mott–Gurney equation:[10]

$$\mu = 8JL^3/9\varepsilon_0\varepsilon V^2 \quad (4)$$

where J/V^2 is the slope of J versus V^2 in Child's regime in Figure 5c. The charge mobility of $MA_3Bi_2I_9$ thin film was calculated to be 3.47×10^{-7} $cm^2\,V^{-1}\,s^{-1}$. Here, the high trap-state density and low charge mobility in $MA_3Bi_2I_9$ thin film may originate from the small $MA_3Bi_2I_9$ grain size derived from this film fabrication method.

On the basis of the characterization above, we concluded that the relatively high exciton binding energy, short carrier diffusion length, high trap-state density, and low charge mobility in $MA_3Bi_2I_9$ thin film were mainly responsible for the low FF in solar cell devices. Although the uniform and compact $MA_3Bi_2I_9$ thin film fabricated in this work promoted V_{oc} over 0.8 V, it is still necessary to explore new ideas to further improve the device performance. Because the exciton binding energy of the $MA_3Bi_2I_9$ material is inherently high, reducing the surface trapping state with suitable interfacial layer or introducing electron acceptor material to form bulk heterojunction structure would be reasonably accessible.[36]

In conclusion, a novel two-step evaporation–spin-coating strategy has been developed to fabricate the $MA_3Bi_2I_9$ thin film with pinhole-free, uniform, and compact surface morphology. The XRD pattern of in situ transformed $MA_3Bi_2I_9$ thin film showed preferred orientation, and the RMS roughness of the film was only 13.23 nm. The superior $MA_3Bi_2I_9$ thin film promoted the inverted PHJ photovoltaic device with champion PCE of 0.39%. Most importantly, the V_{oc} of 0.83 V is the highest value to date among the state-of-art $MA_3Bi_2I_9$-based photovoltaic devices. PL and SCLC measurement revealed that the low FF of the device was caused by the short carrier diffusion length, high trap-state density, and low charge mobility in the $MA_3Bi_2I_9$ thin film. This work proves that the film morphology engineering is crucial for enhancing the optoelectronic performance of lead-free PHJ organohalide solar cells. Further improvements in the FF of the device would boost the PCE in this system, where bulk heterojunction architecture and a suitable interfacial layer could be deeply investigated.

DOI: 10.1021/acs.jpclett.6b02578
J. Phys. Chem. Lett. 2017, 8, 394−400

EXPERIMENTAL SECTION

Perovskite Film and Device Fabrication. PEDOT:PSS (Clevios Al4083), BiI_3, and MAI were purchased from Borun New Material Technology, Ltd. The cleaning process of the ITO-coated glass can be found in our recent report.[37] PEDOT:PSS/deionized water (v/v = 1/3) solutions by sonication and filtering were first spin-coated onto the substrate at 1000 rpm for 60 s and annealed 20 min at 120 °C. Then BiI_3 with various thicknesses was thermal evaporated on the substrate under 10^{-5} mbar vacuum. After that, MAI solutions in isopropanol (IPA) with various concentrations were spin-coated on the top of BiI_3 layer at 4000 rpm for 30 s in a glovebox. The film was allowed to anneal at 120 °C for 1−5 h to form the $MA_3Bi_2I_9$ film. IPA was loaded on the substrate and spin-coated to remove the residual MAI on the film after annealing. To further fabricate the perovskite solar cell device, C_{60} (30 nm), BCP (8 nm), and Ag (120 nm) were sequentially evaporated onto the $MA_3Bi_2I_9$ film.

Film Characterization. Field emission scanning electron microscopy (Quanta 250, FEI, United States) and atomic force microscopy (Solver P47H-PRO, NT-MDT, Russia) were used to investigate the morphology of the $MA_3Bi_2I_9$ film. XRD measurements were performed with a X-ray diffractometer (D/MAX-2400, Rigaku, Japan) with Cu Kα radiation. The absorption spectra were acquired on a UV−vis spectrophotometer (U-3010, Hitachi High-Technologies, Japan). The PL spectra were acquired on a photoluminescence spectroscopy (Fluoromax 4, HORIBA Jobin Yvon, United States).

Device Characterization. All the devices were tested in an Ar-filled glovebox using a Keithley 2400 source meter and a Newport Oriel sol 2A solar simulator (300 W). The light intensity was calibrated to be 100 mW cm^{-2} using a calibrated Si solar cell and a KG5 color filter. The device performance parameters were obtained from the $J-V$ curves of the solar cells under illumination. The incident photon-to-current efficiency (IPCE) was measured on a solar cell measurement system from PV Measurement Inc. We used the 91150 V Reference Cell and Meter (ORIEL instrument) to calibrate the light intensity prior to device testing.

ASSOCIATED CONTENT

Supporting Information

The Supporting Information is available free of charge on the ACS Publications website at DOI: 10.1021/acs.jpclett.6b02578.

SEM with lower magnification, top-down resistance, XRD pattern, UV−vis data, band gap estimation of BiI_3 and $MA_3Bi_2I_9$ films, and device reproducibility (PDF)

AUTHOR INFORMATION

Corresponding Author

*E-mail: zhaoxinwu@mail.xjtu.edu.cn.

ORCID

Zhaoxin Wu: 0000-0003-2979-3051

Author Contributions

†C.R. and Z.W. contributed equally to the work.

Notes

The authors declare no competing financial interest.

ACKNOWLEDGMENTS

This work was financially supported by Basic Research Program of China (2013CB328705), National Natural Science Foundation of China (Grant 11574248, 61275034), Ph.D. Programs Foundation of Ministry of Education of China (Grant 20130201110065), International Cooperation by Shaanxi (Grant 2015KW-008), China Postdoctoral Science Foundation (Grant 2016M590947), and the Fundamental Research Funds for the Central Universities(Grant xjj2016031). The SEM and TEM work was done at International Center for Dielectric Research (ICDR), Xi'an Jiaotong University, Xi'an, China.

REFERENCES

(1) Kojima, A.; Teshima, K.; Shirai, Y.; Miyasaka, T. Organometal Halide Perovskites as Visible-Light Sensitizers for Photovoltaic Cells. *J. Am. Chem. Soc.* **2009**, *131*, 6050−6051.

(2) Saliba, M.; Matsui, T.; Domanski, K.; Seo, J. Y.; Ummadisingu, A.; Zakeeruddin, S. M.; Correa-Baena, J. P.; Tress, W. R.; Abate, A.; Hagfeldt, A.; et al. Incorporation of Rubidium Cations into Perovskite Solar Cells Improves Photovoltaic Performance. *Science* **2016**, *354*, 206−209.

(3) Babayigit, A.; Ethirajan, A.; Muller, M.; Conings, B. Toxicity of Organometal Halide Perovskite Solar Cells. *Nat. Mater.* **2016**, *15*, 247−251.

(4) Leijtens, T.; Eperon, G. E.; Noel, N. K.; Habisreutinger, S. N.; Petrozza, A.; Snaith, H. J. Stability of Metal Halide Perovskite Solar Cells. *Adv. Energy Mater.* **2015**, *5*, 1500963.

(5) Noel, N. K.; Stranks, S. D.; Abate, A.; Wehrenfennig, C.; Guarnera, S.; Haghighirad, A. A.; Sadhanala, A.; Eperon, G. E.; Pathak, S. K.; Johnston, M. B.; et al. Lead-Free Organic−Inorganic Tin Halide Perovskites for Photovoltaic Applications. *Energy Environ. Sci.* **2014**, *7*, 3061−3068.

(6) Lee, S. J.; Shin, S. S.; Kim, Y. C.; Kim, D.; Ahn, T. K.; Noh, J. H.; Seo, J.; Seok, S. I. Fabrication of Efficient Formamidinium Tin Iodide Perovskite Solar Cells through SnF_2−Pyrazine Complex. *J. Am. Chem. Soc.* **2016**, *138*, 3974−3977.

(7) Park, B. W.; Philippe, B.; Zhang, X.; Rensmo, H.; Boschloo, G.; Johansson, E. M. J. Bismuth Based Hybrid Perovskites $A_3Bi_2I_9$ (A: Methylammonium or Cesium) for Solar Cell Application. *Adv. Mater.* **2015**, *27*, 6806−6813.

(8) Eckhardt, K.; Bon, V.; Getzschmann, J.; Grothe, J.; Wisser, F. M.; Kaskel, S. Crystallographic Insights into $(CH_3NH_3)_3(Bi_2I_9)$: A New Lead-Free Hybrid Organic-Inorganic Material as a Potential Absorber for Photovoltaics. *Chem. Commun.* **2016**, *52*, 3058−3060.

(9) Hoye, R. L. Z.; Brandt, R. E.; Osherov, A.; Stevanović, V.; Stranks, S. D.; Wilson, M. W. B.; Kim, H.; Akey, A. J.; Perkins, J. D.; Kurchin, R. C.; et al. Methylammonium Bismuth Iodide as a Lead-Free, Stable Hybrid Organic−Inorganic Solar Absorber. *Chem. - Eur. J.* **2016**, *22*, 2605−2610.

(10) Abulikemu, M.; Ould-Chikh, S.; Miao, X.; Alarousu, E.; Murali, B.; Ndjawa, G. O. N.; Barbé, J.; Labban, A. E.; Amassian, A.; Gobbo, S. D. Optoelectronic and Photovoltaic Properties of the Air-Stable Organohalide Semiconductor $(CH_3NH_3)_3Bi_2I_9$. *J. Mater. Chem. A* **2016**, *4*, 12504−12515.

(11) Lyu, M.; Yun, J. H.; Cai, M.; Jiao, Y.; Bernhardt, P. V.; Zhang, M.; Wang, Q.; Du, A.; Wang, H.; Liu, G.; et al. Organic−Inorganic Bismuth (III)-Based Material: A Lead-Free, Air-Stable and Solution-Processable Light-Absorber beyond Organolead Perovskites. *Nano Res.* **2016**, *9*, 692−702.

(12) Öz, S.; Hebig, J. C.; Jung, E.; Singh, T.; Lepcha, A.; Olthof, S.; Jan, F.; Gao, Y.; German, R.; Loosdrecht, P. H. M.; et al. Zero-Dimensional $(CH_3NH_3)_3Bi_2I_9$ Perovskite for Optoelectronic Applications. *Sol. Energy Mater. Sol. Cells* **2016**, *158*, 195−201.

(13) Singh, T.; Kulkarni, A.; Ikegami, M.; Miyasaka, T. Effect of Electron Transporting Layer on Bismuth-Based Lead-Free Perovskite $(CH_3NH_3)_3Bi_2I_9$ for Photovoltaic Applications. *ACS Appl. Mater. Interfaces* **2016**, *8*, 14542−14547.

(14) Zhang, X.; Wu, G.; Gu, Z.; Guo, B.; Liu, W.; Yang, S.; Ye, T.; Chen, C.; Tu, W.; Chen, H. Active-Layer Evolution and Efficiency Improvement of $(CH_3NH_3)_3Bi_2I_9$-Based Solar Cell on TiO_2-Deposited ITO Substrate. *Nano Res.* **2016**, *9*, 2921−2930.

DOI: 10.1021/acs.jpclett.6b02578
J. Phys. Chem. Lett. 2017, 8, 394−400

(15) Lehner, A. J.; Fabini, D. H.; Evans, H. A.; Hebert, C. A.; Smock, S. R.; Hu, J.; Wang, H.; Zwanziger, J. W.; Chabinyc, M. L.; Seshadri, R. Crystal and Electronic Structures of Complex Bismuth Iodides $A_3Bi_2I_9$ (A = K, Rb, Cs) Related to Perovskite: Aiding the Rational Design of Photovoltaics. *Chem. Mater.* **2015**, *27*, 7137−7148.
(16) Liu, M.; Johnston, M. B.; Snaith, H. J. Efficient Planar Heterojunction Perovskite Solar Cells by Vapour Deposition. *Nature* **2013**, *501*, 395−398.
(17) Chen, Y.; Chen, T.; Dai, L. Layer-by-Layer Growth of $CH_3NH_3PbI_{3-x}Cl_x$ for Highly Efficient Planar Heterojunction Perovskite Solar Cells. *Adv. Mater.* **2015**, *27*, 1053−1059.
(18) Xi, J.; Wu, Z.; Dong, H.; Xia, B.; Yuan, F.; Jiao, B.; Xiao, L.; Gong, Q.; Hou, X. Controlled Thickness and Morphology for Highly Efficient Inverted Planar Heterojunction Perovskite Solar Cells. *Nanoscale* **2015**, *7*, 10699−10707.
(19) Lin, Q.; Armin, A.; Nagiri, R. C. R.; Burn, P. L.; Meredith, P. Electro-optics of Perovskite Solar Cells. *Nat. Photonics* **2015**, *9*, 106−112.
(20) Malinkiewicz, O.; Yella, A.; Lee, Y. H.; Espallargas, G. M.; Graetzel, M.; Nazeeruddin, M. K.; Bolink, H. J. Perovskite Solar Cells Employing Organic Charge-Transport Layers. *Nat. Photonics* **2014**, *8*, 128−132.
(21) Xiao, Z.; Bi, C.; Shao, Y.; Dong, Q.; Wang, Q.; Yuan, Y.; Wang, C.; Gao, Y.; Huang, J. Efficient, High Yield Perovskite Photovoltaic Devices Grown by Interdiffusion of Solution-Processed Precursor Stacking Layers. *Energy Environ. Sci.* **2014**, *7*, 2619−2623.
(22) Chiang, C. H.; Tseng, Z. L.; Wu, C. G. Planar Heterojunction Perovskite/$PC_{71}BM$ Solar Cells with Enhanced Open-Circuit Voltage via A (2/1)-Step Spin-Coating Process. *J. Mater. Chem. A* **2014**, *2*, 15897−15903.
(23) Ma, F.; Zhou, M.; Jiao, Y.; Gao, G.; Gu, Y.; Bilic, A.; Chen, Z.; Du, A. Single Layer Bismuth Iodide: Computational Exploration of Structural, Electrical, Mechanical and Optical Properties. *Sci. Rep.* **2015**, *5*, 17558.
(24) Tauc, J.; Grigorovici, R.; Vancu, A. Optical Properties and Electronic Structure of Amorphous Germanium. *Phys. Status Solidi B* **1966**, *15*, 627−637.
(25) Brandt, R. E.; Kurchin, R. C.; Hoye, R. L. Z.; Poindexter, J. R.; Wilson, M. W. B.; Sulekar, S.; Lenahan, F.; Yen, P. X. T.; Stevanović, V.; Nino, J. C.; et al. Investigation of Bismuth Triiodide (BiI_3) for Photovoltaic Applications. *J. Phys. Chem. Lett.* **2015**, *6*, 4297−4302.
(26) Sun, S.; Salim, T.; Mathews, N.; Duchamp, M.; Boothroyd, C.; Xing, G.; Sum, T. C.; Lam, Y. M. The Origin of High Efficiency in Low-Temperature Solution-Processable Bilayer Organometal Halide Hybrid Solar Cells. *Energy Environ. Sci.* **2014**, *7*, 399−407.
(27) Lee, E. M. Y.; Tisdale, W. A. Determination of Exciton Diffusion Length by Transient Photoluminescence Quenching and Its Application to Quantum Dot Films. *J. Phys. Chem. C* **2015**, *119*, 9005−9015.
(28) Xing, G.; Mathews, N.; Sun, S.; Lim, S. S.; Lam, Y. M.; Grätzel, M.; Mhaisalkar, S.; Sum, T. C. Long-Range Balanced Electron- and Hole-Transport Lengths in Organic-Inorganic $CH_3NH_3PbI_3$. *Science* **2013**, *342*, 344−347.
(29) Li, Y.; Yan, W.; Li, Y.; Wang, S.; Wang, W.; Bian, Z.; Xiao, L.; Gong, Q. Direct Observation of Long Electron-Hole Diffusion Distance in $CH_3NH_3PbI_3$ Perovskite Thin Film. *Sci. Rep.* **2015**, *5*, 14485.
(30) Stranks, S. D.; Eperon, G. E.; Grancini, G.; Menelaou, C.; Alcocer, M. J.; Leijtens, T.; Herz, L. M.; Petrozza, A.; Snaith, H. J. Electron-Hole Diffusion Lengths Exceeding 1 Micrometer in an Organometal Trihalide Perovskite Absorber. *Science* **2013**, *342*, 341−344.
(31) Wu, X.; Trinh, M. T.; Niesner, D.; Zhu, H.; Norman, Z.; Owen, J. S.; Yaffe, O.; Kudisch, B. J.; Zhu, X.-Y. Trap States in Lead Iodide Perovskites. *J. Am. Chem. Soc.* **2015**, *137*, 2089−2096.
(32) Kawai, T.; Ishii, A.; Kitamura, T.; Shimanuki, S.; Iwata, M.; Ishibashi, Y. Optical Absorption in Band-Edge Region of $(CH_3NH_3)_3Bi_2I_9$ Single Crystals. *J. Phys. Soc. Jpn.* **1996**, *65*, 1464−1468.
(33) Yang, D.; Zhou, X.; Yang, R.; Yang, Z.; Yu, W.; Wang, X.; Li, C.; Liu, S.; Chang, R. P. H. Surface Optimization to Eliminate Hysteresis for Record Efficiency Planar Perovskite Solar Cells. *Energy Environ. Sci.* **2016**, *9*, 3071−3078.
(34) Shao, Y.; Xiao, Z.; Bi, C.; Yuan, Y.; Huang, J. Origin and Elimination of Photocurrent Hysteresis by Fullerene Passivation in $CH_3NH_3PbI_3$ Planar Heterojunction Solar Cells. *Nat. Commun.* **2014**, *5*, 5784.
(35) Saidaminov, M. I.; Adinolfi, V.; Comin, R.; Abdelhady, A. L.; Peng, W.; Dursun, I.; Yuan, M.; Hoogland, S.; Sargent, E. H.; Bakr, O. M. Planar-Integrated Single-Crystalline Perovskite Photodetectors. *Nat. Commun.* **2015**, *6*, 8724.
(36) Ran, C.; Chen, Y.; Gao, W.; Wang, M.; Dai, L. One-Dimensional (1D) [6,6]-Phenyl-C_{61}-Butyric Acid Methyl Ester (PCBM) Nanorods as An Efficient Additive for Improving the Efficiency and Stability of Perovskite Solar Cells. *J. Mater. Chem. A* **2016**, *4*, 8566−8572.
(37) Xi, J.; Wu, Z.; Xi, K.; Dong, H.; Xia, B.; Lei, T.; Yuan, F.; Wu, W.; Jiao, B.; Hou, X. Initiating Crystal Growth Kinetics of α-$HC(NH_2)_2PbI_3$ for Flexible Solar Cells with Long-Term Stability. *Nano Energy* **2016**, *26*, 438−445.

DOI: 10.1021/acs.jpclett.6b02578
J. Phys. Chem. Lett. 2017, 8, 394−400